



PII S0016-7037(02)00947-X

X-ray absorption fine structure determination of pH-dependent U-bacterial cell wall interactions

S. D. KELLY,¹ K. M. KEMNER,^{1,*} J. B. FEIN,² D. A. FOWLE,^{2,†} M. I. BOYANOV,^{1,2} B. A. BUNKER,² and N. YEE¹¹Argonne National Laboratory, Argonne, IL60439, USA²University of Notre Dame, Civil Engineering and Geological Sciences, Notre Dame, IN46556, USA

(Received September 21, 2001; accepted in revised form April 23, 2002)

Abstract—X-ray absorption fine structure (XAFS) measurements was used at the U L3-edge to directly determine the pH dependence of the cell wall functional groups responsible for the absorption of aqueous UO_2^{2+} to *Bacillus subtilis* from pH 1.67 to 4.80. Surface complexation modeling can be used to predict metal distributions in water–rock systems, and it has been used to quantify bacterial adsorption of metal cations. However, successful application of these models requires a detailed knowledge not only of the type of bacterial surface site involved in metal adsorption/desorption, but also of the binding geometry. Previous acid-base titrations of *B. subtilis* cells suggested that three surface functional group types are important on the cell wall; these groups have been postulated to correspond to carboxyl, phosphoryl, and hydroxyl sites. When the U(VI) adsorption to *B. subtilis* is measured, observed is a significant pH-independent absorption at low pH values (<3.0), ascribed to an interaction between the uranyl cation and a neutrally charged phosphoryl group on the cell wall. The present study provides independent quantitative constraints on the types of sites involved in uranyl binding to *B. subtilis* from pH 1.67 to 4.80. The XAFS results indicate that at extremely low pH (pH 1.67) UO_2^{2+} binds exclusively to phosphoryl functional groups on the cell wall, with an average distance between the U atom and the P atom of 3.64 ± 0.01 Å. This U-P distance indicates an inner-sphere complex with an oxygen atom shared between the UO_2^{2+} and the phosphoryl ligand. The P signal at extremely low pH value is consistent with the UO_2^{2+} binding to a protonated phosphoryl group, as previously ascribed. With increasing pH (3.22 and 4.80), UO_2^{2+} binds increasingly to bacterial surface carboxyl functional groups, with an average distance between the U atom and the C atom of 2.89 ± 0.02 Å. This U-C distance indicates an inner-sphere complex with two oxygen atoms shared between the UO_2^{2+} and the carboxyl ligand. The results of this XAFS study confirm the uranyl-bacterial surface speciation model. Copyright © 2002 Elsevier Science Ltd

1. INTRODUCTION

Laboratory and field studies have demonstrated that bacterial cell walls efficiently adsorb a variety of aqueous metal cations (Beveridge and Murray, 1976; Gonçalves et al., 1987; Harvey and Leckie, 1985; Konhauser et al., 1993). Therefore, because bacteria are abundant in near-surface geologic systems, bacterial adsorption reactions can significantly affect metal mobilities in aqueous systems (Harvey et al., 1982; Ledin et al., 1999). The extent of adsorption of aqueous metals onto bacterial surfaces can vary markedly with changing conditions such as pH, ionic strength, and fluid composition (Ferris et al., 1989; Fein et al., 1997; Daughney et al., 1998; Fein and Delea, 1999; Fowle and Fein, 1999; Small et al., 1999, 2001). The effects of these changing conditions on adsorption/desorption reactions can be quantified by using one of two different approaches: partitioning relationships or surface complexation models. A number of studies have used partitioning approaches to model metal adsorption onto bacteria (Ferris et al., 1989; Mullen et al., 1989; Small et al., 1999, 2001; Beolchini et al., 2001). In view of the complexities associated with natural systems, partitioning adsorption models are relatively simple to apply because they do not require a detailed understanding of the nature of the

surfaces or adsorption mechanisms involved. That is, the extent of adsorption can be measured directly on a sample of material from the field, and a bulk partition coefficient can be determined that describes the distribution of the species of interest between the bacterial surface and the other phase or phases of interest. However, partition coefficient values under conditions not studied in the laboratory cannot be estimated theoretically from a set of measured partition coefficient values. Partition coefficient models cannot predict the distribution of metals in systems not previously studied.

Surface complexation models, which apply the formalism of aqueous ion association reactions to solute adsorption reactions with surfaces, require a detailed understanding not only of the surfaces involved, but also of the adsorption/desorption mechanisms. A surface complexation model treats the adsorbed metal as another metal species whose stability can be quantified with an equilibrium constant. By knowing all of the important reactions that exist in a system (and their stoichiometries), as well as the values of their equilibrium constants, the distribution of metals between various reservoirs (in aqueous solution, on mineral surfaces, on bacterial surfaces) can be explicitly calculated. The equilibrium constants that describe the extent of adsorption in surface complexation models are invariant with respect to most of the parameters affecting partition coefficients (Bethke and Brady, 2000; Koretsky, 2000).

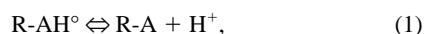
The surface complexation approach can be used to quantify bacterial adsorption of metal cations (Plette et al., 1995; Fein et

* Author to whom correspondence should be addressed (skelly@anl.gov).

† Present address: University of Windsor, Great Lakes Institute for Environment Research, Windsor, ON N9B 3P4.

al., 1997; He and Tebo, 1998; Fowle et al., 2000). For example, Fein et al. (1997) used acid-base titrations of *Bacillus subtilis* suspensions to determine acidity constants for the important surface functional groups and metal adsorption experiments to yield site-specific stability constants for the metal-bacterial surface complexes. However, these and subsequent batch adsorption experiments provide only circumstantial evidence regarding the mechanism of adsorption (or the stoichiometry of the adsorption reaction). Clearly, successful application of a surface complexation approach to quantifying bacterial adsorption of aqueous metal cations requires a detailed understanding of the binding mechanism. That information can be provided directly by using X-ray absorption fine structure (XAFS) spectroscopy.

Gram-positive cell walls are constructed of linear polymers of peptidoglycan covalently linked together around the cell membrane. The peptidoglycan forms a single giant macromolecule (~25 nm thick) rich in carboxyl and hydroxyl functional groups. The gram-positive cell wall is also composed of secondary polymers (e.g., teichoic acid) having phosphoryl functional groups (Beveridge and Murray, 1976, 1980). Numerous studies have shown that bacterial surfaces display pH-dependent charging and acid-base characteristics (Harden and Harris, 1953; Plette et al., 1995; Fein et al., 1997; Cox et al., 1999). These surface characteristics are controlled by the proton-active functional groups found on the cell wall. The surface complexation approach employed by Fein et al. (1997) models the acidity of these surface functional groups by using the equilibrium equation



where R denotes the bacterium to which each functional group type, A, is attached. The distribution of protonated and deprotonated sites can be quantified with the corresponding mass action equation

$$K_a = [\text{R-A}][\text{H}^{+}]/[\text{R-AH}^{\circ}]. \quad (2)$$

Here, $[\text{R-A}^{-}]$ and $[\text{R-AH}^{\circ}]$ represent the concentration of deprotonated and protonated surface species, respectively, and $[\text{H}^{+}]$ represents the activity of protons in solution. The notation pK_a represents the negative logarithm of the value of the equilibrium constant, K_a , for reaction 1. The data of Fein et al. (1997), Daughney et al. (1998), and Yee and Fein (2001) demonstrate that models involving three distinct types of surface organic acid functional groups (each with its own discrete pK_a value) provide an excellent fit to the observed protonation/deprotonation behavior of a wide range of bacterial species. Fein et al. (1997) reported pK_a values of 4.82, 6.9, and 9.4 for *B. subtilis* and postulated that the active surface functional groups correspond to carboxyl, phosphoryl, and hydroxyl groups, respectively. Cox et al. (1999) reported five pK_a values, ranging from 5.2 to 10.0. The spectroscopic data described in this study are independent of these bacterial surface charging models and can be used to provide some constraints on the bacterial surface functional groups responsible for binding under the experimental conditions.

Fein et al. (1997) observed negligible Cd, Cu, and Pb adsorption to *B. subtilis* under low-pH conditions, with adsorption increasing with increasing pH above approximately pH 3.0 as

the surface functional groups are successively deprotonated. Fowle et al. (2000) observed similar pH dependence for UO_2^{+2} adsorption to the same bacteria, along with significant uranyl adsorption even under low-pH conditions. The low-pH adsorption was ascribed to an interaction between the uranyl cation and a neutrally charged phosphoryl group on the cell wall. However, all of these models are based only on bulk adsorption data, and the nature and mechanism of metal binding to the cell walls have not been determined. XAFS measurements at the complexed metal absorption edge can distinguish between the different functional groups proposed to be important in metal uptake, thereby providing additional independent constraints on the stoichiometry of the adsorption reactions.

A number of U XAFS studies have investigated the interactions between U(VI) and solutions (Allen et al., 1995, 1996, 1997; Thompson et al., 1995, 1997; Docrat et al., 1999; Hay et al., 2000); sediments, soils, and soil constituents (Dent et al., 1992; Morris et al., 1996; Reich et al., 1996; Sturchio et al., 1998; Barger et al., 2000; Duff et al., 2000; Reeder et al., 2000); fungal biomass (Sarret et al., 1998); halophilic bacteria (Francis et al., 1998); and the gram-positive bacterium *B. subtilis* (Hennig et al., 2000). Other studies have used indirect methods, such as spectrophotometric and potentiometric measurements, to investigate the interaction between U and other heavy metals with *Zoogloea ramigera* biomass (Norber and Persson, 1984). However, to our knowledge, no systematic study of the pH-dependent sorption of U to bacterial cell membranes has been undertaken.

2. METHODS

2.1. Experimental Procedures

Suspensions of *B. subtilis* in 0.1 mol/L NaClO_4 were exposed to aqueous U solutions and allowed to equilibrate for 2 h, as determined sufficient by Fowle et al. (2000), under three different pH conditions. Samples U11, U12, and U13 contained 83 μm of U(VI) and 1.5 g (wet weight) of bacteria per liter at pH values of 1.67, 3.22, and 4.80, respectively. Samples Uh1, Uh2, and Uh3, respectively, contained 210 μm of U(VI) and 1.5 g (wet weight) of bacteria per liter at the same pH values. Biomass and sample preparation details were identical to those employed by Fowle et al. (2000). The pH values studied here cover the range examined by those authors. These samples therefore enable the use of XAFS for the determination of the different metal binding mechanisms that are responsible for the adsorption behavior observed by Fowle et al. (2000) over this pH range. After equilibration between the uranyl-bearing aqueous solution and the biomass, each experimental system was centrifuged at 10,000 g for 60 min, and the supernatant was removed. Fluorescence U $L_{3\text{-edge}}$ XAFS measurements were made on the wet, homogeneous biomass. The XAFS measurements were performed at the MRCAT sector 10-ID beamline (Segre et al., 2000) at the Advanced Photon Source.

The beamline optics and setup parameters for the U $L_{3\text{-edge}}$ XAFS measurements were as follows. The undulator was tapered by approximately 2 keV to reduce the variation in the incident intensity to less than 15% over the scanned energy range. The energy of the incident X-rays was scanned by using the Si(111) reflection of the double-crystal monochromator

running on the third harmonic of the beamline undulator. Higher harmonics were rejected with a Rh mirror. The incident and transmitted X-ray ion chambers were both filled with nitrogen gas. The fluorescence detector in the Stern-Heald geometry (Stern and Heald, 1983) was filled with Ar gas, and a Sr filter of three absorption lengths was used to reduce the background signal. The incident X-ray beam profile was 0.7 mm square. Linearity tests (Kemner et al., 1994) indicated less than 0.3% nonlinearity for a 50% decrease in incident X-ray intensity.

The results from the analysis of several solution standards are the foundation for the analysis of the U biomass data. The uranyl cations in the standards and the uranyl adsorbed to the biomass are likely to have similar local U atomic structure. From each standard, we gain well-characterized, isolated information of the interaction of uranyl with water, acetate, and phosphate groups. The hydrated uranyl standard provides a baseline view of the uranyl cation, and the acetate and phosphate standards represent the carboxyl and phosphoryl functional groups, respectively, in the biomass samples. This information is combined to constrain a model of the binding mechanism or mechanisms that control uranyl adsorption to biomass. In each model tested, we consider the uranyl bound to any combination of atoms (C, P, and/or H) in the second coordination shell, because of the attachment to different cell wall functional groups. Additionally, data from the standards were analyzed to assess the ability of FEFF7 (Zabinsky et al., 1995), a theoretical XAFS modeling code, to accurately model the uranyl cation's local chemical environment.

The aqueous uranyl standards include hydrated uranyl, uranyl acetate, and uranyl phosphate solutions. All uranyl standards were prepared by using a 1000-ppm uranyl nitrate stock solution. The hydrated uranyl sample (U-H₂O) was prepared by diluting the stock solution with deionized water. The standard had a final solution pH of 0.96. The uranyl acetate standard (U-C) was prepared by adding glacial acetic acid to the uranyl stock solution to achieve an acetate:U ratio of 100:1, then adjusting the final pH to 4.4 with NaOH. The uranyl phosphate standard (U-P) was prepared by adding concentrated phosphoric acid to the uranyl stock solution to achieve a phosphate:U ratio of 100:1, with a final pH of 1.5. The final U concentrations are ~2.9 and 3.4 mM for the U-P and U-C samples. Aqueous species calculations by FITEQL (Westall, 1982) in conjunction with the thermodynamic data of Grenthe et al. (1992) and Smith et al. (1997) for the U-C and U-P standard solutions indicate 11% UO₂(Ac), 42% UO₂(Ac)₂, 46% UO₂(Ac)₃, and 1% other species for the U-C standard and 46% UO₂(H₂PO₄), 48% UO₂(H₂PO₄)₂ and 6% other species for the U-P standard. These percentages indicate that the average number of near-neighbor C and P atoms to the uranyl in the U-C and U-P standards are ~2.33 and ~1.42, respectively. The X-ray absorption near-edge structure (XANES) standards include powder uraninite (UO₂) and γ -UO₃ purchased from Alfa Aesar, diluted approximately 1 to 100 in SiO₂ and measured in fluorescence mode. X-ray diffraction measurements indicate that the purity levels of the crystal phases of the XANES standards are ~95% uraninite (UO₂) for the U(IV) standard and ~95% γ -UO₃ for the U(VI) standard.

2.2. XAFS Analysis

2.2.1. XANES

Two energy scans were collected at three different locations on the sample to reduce radiation exposure. The sample was exposed for approximately 1 min for each of the scans at each location. Measuring two spectra at each location enabled determination of radiation-induced chemical effects at the 1-min timescale. No time-dependent change in the data was observed for any of the samples.

XANES is useful in determining the average valence state of U adsorbed to the biomass samples. The energy position of the edge step is directly related to the valence state of the uranium. Therefore, careful monitoring of the monochromator energy is paramount for making these comparisons. We used the transmission XAFS signal of a Y-foil as described elsewhere (Cross and Frenkel, 1998), as a reference for accurately aligning the edge energy positions of U(IV) (UO₂) and U(VI) (UO₃) powder standards, along with the U biomass data. The edge positions for the U(IV) and U(VI) standards differed by approximately 4.3 eV, as determined by the energy value at half the step height of the normalized data. For the 0.7-mm vertical beam size used in these experiments, the line width of the monochromator at 17 keV is ~4.0 eV. Additionally, the step accuracy of the monochromator at 17 keV is ± 0.13 eV (A. J. Kropf, private communication). For our experiments, the limiting factor in determining the valence state of the U in the biomass sample is purity of the XANES standards. A generous estimation of the uncertainty in the U valence state determination is $\pm 10\%$.

2.2.2. Extended XAFS

Detailed discussions of extended XAFS (EXAFS) theory can be found elsewhere (Stern and Heald, 1983). Here we give an overview of EXAFS spectroscopy and its role in determining the average atomic environment of the U atoms in these samples. The EXAFS signal for a particular element in a sample is the oscillatory part of the X-ray absorption coefficient above the adsorption edge of that element and can be written as the sum of the contributions from each path (*i*) of the photoelectron, generated by the absorption of an X-ray by the atom, as it scatters from the atoms surrounding the U atoms. It is useful to group the paths by symmetry by multiplying the individual contributions to the EXAFS signal by the degeneracy of each path N_{degen} . For the special case of a single-scattering event, N_{degen} represents the number of atoms in a shell about the U atoms.

The theoretical EXAFS models are constructed by the program FEFF7 (Zabinsky et al., 1995) on the basis of the crystal structure of uranyl acetate (Templeton et al., 1985) and hydrogen uranyl phosphate tetrahydrate (Morosin, 1978). Overlapping muffin-tin spheres were used in the FEFF7 calculation as reported previously (Hudson et al., 1995). FEFF7 calculates the values for $F_i(k)$, $\delta_i(k)$, and $\lambda(k)$, which are the effective scattering amplitude, the effective scattering phase shift, and the mean free path of the photoelectron, respectively. These variables depend on *k*, the photoelectron wave number, and are related to energy of the photoelectron (*E*) through the relationship $k^2 = 2m(E - E_0)/\hbar$. Here, *m* is the mass of an electron, E_0

Table 1. Fit range, ΔR ; data range, Δk ; number of independent points in the fit, N_{idp} ; number of variables determined in the fit, N_{var} ; degrees of freedom in the fit, ν ; reduced-chi-squared value, χ_{γ}^2 ; and r factor, R .^a

Sample	Model	ΔR (Å)	Δk (Å ⁻¹)	N_{idp}	N_{var}	ν	χ_{γ}^2	R %
U-H ₂ O	Hydrated	[1.0–3.2]	[2.0–10.7]	14	7	7	10	0.5
U-C	Acetate	[1.0–4.2]	[2.5–11.7]	20	14	6	9	0.5
U-P	Phosphate	[1.1–4.0]	[2.8–14.0]	22	13	9	8	1.6
Uh1, Uh2, Uh3	Biomass	[1.0–3.8]	[2.0–13.5]	20	9	11	33	0.9
U11, U12, U13	Biomass	[1.0–3.8]	[2.0–13.5]	20	9	11	37	0.6

^a Data were processed with k weight = 1, 2, and 3 in the Fourier transform. Full width of the Hanning window sill, $dk = 1 \text{ Å}^{-1}$.

is the Fermi energy, and \hbar is Plank's constant. The structural EXAFS parameters that are often determined by a fit to data are N_{degen} (degeneracy of the path), ΔR_i (change in the half-path length), σ_i^2 (relative mean square displacement about the equilibrium path length), S_0^2 (passive electron reduction factor), and ΔE_0^1 (energy shift of the photoelectron). The parameters determined in the fits to the data are discussed in more detail in the following sections. The value for the EXAFS parameter S_0^2 was found to converge to 1.0 ± 0.10 for all U L3-EXAFS standard and biomass data. Therefore, S_0^2 was held to that value for all models.

Fits to the EXAFS data are made in R-space and obtained by taking the Fourier transform (FT) of $\chi(k)$. Because the EXAFS signal depends on $\sin[2kR_i + \delta_i(k)]$, a maximum in $|\text{FT } \chi(R)|$ amplitude occurs at positions close to the half-path length, R_i . In this work, we refer to the crystallographic positions of the atoms in terms of their actual distance in Å from the U atoms and their contribution to the Fourier transform of the data in terms of the distance in Å uncorrected for the photoelectron phase shift, $\delta_i(k)$. For example, a crystallographic position resulting in a U→O path of 2.3 Å will have a maximum contribution to the Fourier transform of the data at approximately 1.9 Å. (For a more detailed discussion of the photoelectron phase shift, see Stern and Heald, 1983.)

The data were analyzed by the codes from the UWXAFS package (Stern et al., 1995). These programs include AUTOBK (Newville et al., 1993) to remove the background, FEFFIT (Newville et al., 1995) to fit the theoretical model to the EXAFS data, and FEFF7 (Zabinsky et al., 1995) to create the theoretical model. The data sets were aligned and the backgrounds were removed by the AUTOBK program. The input parameter to AUTOBK that determines the maximum frequency of the background R_{bkg} was set to 0.8 Å. Two EXAFS measurements were taken at three different spots, for a total of six measurements. The resulting six $\chi(k)$ data sets were averaged. FEFFIT can also adjust the background in the fit and report the correlation between the background and the structural-fit parameters. We found that this correlation was always less than 60%, indicating that the background was not significantly affecting the structural-fit parameters. The fits were performed in R-space obtained by taking the Fourier transform of the $\chi(k)$ data. The data and fit ranges, along with the goodness-of-fit parameters, are listed in Table 1.

The definitions of the goodness-of-fit values for EXAFS data analysis are not standardized, and therefore they are given here. The goodness-of-fit values are the EXAFS reliability factor, R , and the reduced χ^2 value, χ_{γ}^2 . Here, γ is the number of degrees of freedom in the fit, given by the number of independent

points, N_{idp} , in the fit, minus the number of parameters determined in the fit (Stern, 1993).

The value for χ_{γ}^2 is normalized by the uncertainty in the measurement and has both statistical and systematic contributions. The contribution to the uncertainty from statistical noise can be obtained by measuring the fluctuations in R-space between 15 and 25 Å. If the uncertainties are purely random with no systematic error, the χ_{γ}^2 value is expected to be close to one. Typically, however, the χ_{γ}^2 value is much larger. This could indicate either an incorrect model or dominance of systematic errors. To identify the sources of uncertainties, an EXAFS reliability factor, R , is calculated. The reliability factor is the sum of the differences between the model value and data squared, divided by the sum of the squares of the data. Good fits occur for R values of a few percent. With such values of R , the large value for χ_{γ}^2 can confidently be attributed to systematic errors. The quoted uncertainties in fitted parameters are multiplied by χ_{γ}^2 to correct for an underestimation of the uncertainties in the value for χ_{γ}^2 .

3. RESULTS

3.1. XANES

An example of the aligned and normalized absorption data from the standards and U biomass at pH = 1.67 is shown in Figure 1. The data clearly indicate that the U(VI) added to the biomass solution was not reduced to U(IV) by either the bacterial biomass or X-ray radiation, because the edge position is

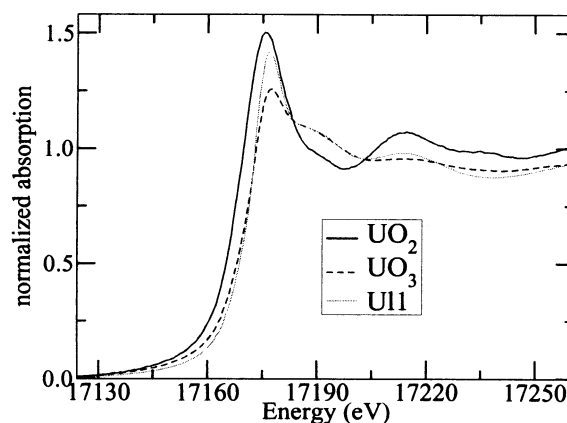


Fig. 1. Normalized adsorption data for U(VI) and U(IV) standards UO_3 and UO_2 , respectively, and U11 data.

Table 2. Description of the paths included in the models followed by their parameterization in terms of the XAFS parameters determined in the fit to the uranyl standards.

Path ^a	R (Å) ^b	N _{degen} ^c	Amp ^d (%)	N _{degen}	ΔR _i	σ ²	ΔE _{0i}
U→Oax	1.76	1	100	2	ΔR ₁	σ ₁ ²	ΔE ₀₁
U→Oeq	2.45	1	100	N ₂	ΔR ₂	σ ₂ ²	ΔE ₀₂
U→Oeq ^e	2.33	1	100	N ₃	ΔR ₃	σ ₂ ²	ΔE ₀₂
U→C1 ^f	2.85	3	53	N ₄	ΔR ₄	σ ₄ ²	ΔE ₀₃
U→Oeq→C1 ^f	3.29	12	30	4 × N ₄	ΔR ₅	σ ₅ ²	0.5 × ΔE ₀₂ + 0.5 × ΔE ₀₃
U→Oax1→U→Oax1	3.52	2	20	2	2 × ΔR ₁	2 × σ ₁ ²	ΔE ₀₁
U→Oax1→Oax2	3.52	2	17	2	2 × ΔR ₁	2 × σ ₁ ²	ΔE ₀₁
U→Oax2→U→Oax1	3.52	2	28	2	2 × ΔR ₁	2 × σ ₁ ²	ΔE ₀₁
U→p ^e	3.60	4	32	N ₆	ΔR ₆	σ ₆ ²	ΔE ₀₂
U→Oeq→P ^e	3.72	8	26	2 × N ₆	ΔR ₆	σ ₆ ²	ΔE ₀₂
U→C2 ^f	4.35	3	13	N ₄	ΔR ₇	σ ₇ ²	ΔE ₀₃
U→C1→C2 ^f	4.35	6	33	2 × N ₄	ΔR ₇	σ ₇ ²	ΔE ₀₃
U→C1→C2→C1 ^f	4.35	6	20	N ₄	ΔR ₇	σ ₇ ²	ΔE ₀₃

^a Atom types in the scattering path.

^b Initial path length from the theoretical models.

^c Degeneracy from the theoretical models.

^d Amplitude ratio relative to the first path, with assumed degeneracy calculated by FEFF7.

^e Additional paths for the uranyl phosphate standard.

^f Additional paths for the uranyl acetate standard.

consistent with the U(VI) standard and not the U(IV) standard. The U XANES data from these experiments indicate a single U(VI) valence state.

3.2. EXAFS

Each of the reference compounds is closely related to the others and to the U biomass data. The signal from uranyl is expected to be a part of the signal in each of the other data sets. Therefore, the hydrated uranyl model is used as a starting point for each of the other models.

3.2.1. Hydrated uranyl

All scattering paths used and parameters determined in the fit of the hydrated uranyl (U-H₂O) data are listed in Table 2, with the parameters constrained in the fit written in terms of the constraining relationship. This best-fit model for the hydrated uranyl sample consists of two axial oxygen (Oax) atoms and approximately six equatorial oxygen (Oeq) atoms (Table 2), Figure 2 shows the structure of the uranyl moiety, a uranium atom with two closely bound Oax atoms, and approximately six Oeq atoms, which would be the O atoms from the waters of hydration for the hydrated uranyl standard. The acetate/phosphate group also shown in Figure 2 is for the other uranyl aqueous standards. Other studies of crystalline uranyl compounds have reported a split Oax distance of 0.001 to 0.03 Å (Morosin, 1978; Mercier et al., 1984; Templeton et al., 1985). Therefore, two Oax distances were considered but were found to be unnecessary with the XAFS resolution of 0.14 Å determined from the data range listed in Table 1. Multiple-scattering paths from the Oax atoms were found to contribute significantly in the fit region. This result is due partially to the tight binding of the Oax atoms to the U, as determined by the small σ² value (Table 3) and the linearity of the Oax-U-Oax bond. The data and best-fit model for the hydrated uranyl are shown

in Figure 3a and b. The model follows the data well over the entire fit range of 1.0 to 3.2 Å, including the multiple-scattering region (2.5 to 3.2 Å), whereas the parameterization for the multiple-scattering paths was completely determined from the single-scattering U→Oax path (Table 2). The degeneracy

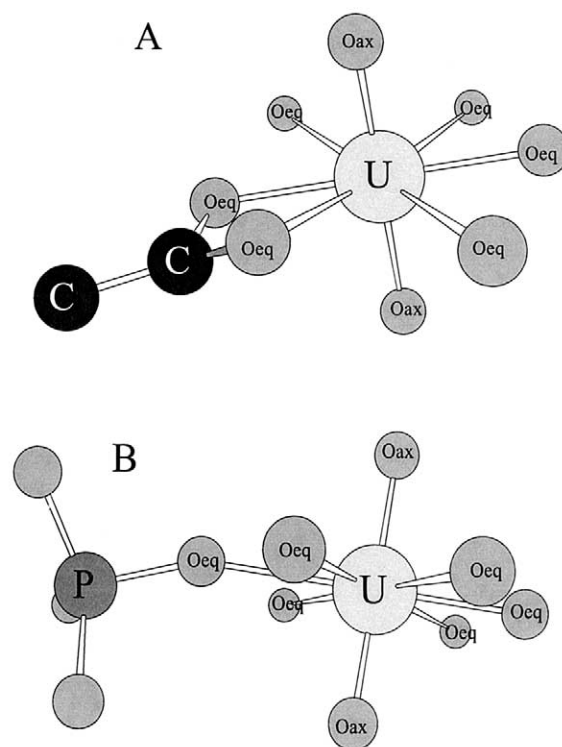


Fig. 2. (A) Bidentate binding of the uranyl to an acetate group. (B) Monodentate binding of the uranyl to a phosphate group.

Table 3. Paths, initial path length (R), and parameters (N_{degen} , ΔR_i , σ_i^2 , ΔE_{0i}) determined in the fit to each series of U biomass data.

Path	R (Å)	N_{degen}	ΔR_i (Å)	σ_i^2 (Å ²)	ΔE_{0i}
U→Oax	1.79	2	ΔR_1	σ_1^2	ΔE_{01}
U→Oeq1	2.28	N_2	ΔR_2	σ_2^2	ΔE_{02}
U→Oeq2	2.49	N_3	ΔR_3	σ_3^2	ΔE_{02}
U→C	2.85	N_4	ΔR_4	σ_4^2	ΔE_{02}
U→Oeq→C	3.29	$4 \times N_4$	ΔR_5	σ_4^2	ΔE_{02}
U→Oax→Oax2	3.58	2	$2 \times \Delta R_1$	$2 \times \sigma_1^2$	ΔE_{01}
U→Oax1→U→Oax2	3.58	2	$2 \times \Delta R_1$	$2 \times \sigma_1^2$	ΔE_{01}
U→Oax2→U→Oax1	3.58	2	$2 \times \Delta R_1$	$2 \times \sigma_1^2$	ΔE_{01}
U→P	3.74	N_6	ΔR_6	σ_6^2	ΔE_{02}
U→Oeq→P	3.82	$2 \times N_6$	ΔR_6	σ_6^2	ΔE_{02}

(N_{degen}) of each multiple-scattering path is two because there are two equivalent paths (i.e., U→Oax1→Oax2 and U→Oax2→Oax1 are equivalent paths).

3.2.2. Aqueous uranyl acetate

All scattering paths used and parameters determined in the fit of the aqueous uranyl acetate complex (U-C) standard are listed in Table 2. The uranyl structure with a single acetate group attached is illustrated in Figure 2A. This best-fit model for the uranyl acetate sample consists of two Oax atoms, approximately six Oeq atoms, approximately three carbon (C1) atoms at 2.89 Å and three more carbon (C2) atoms at 4.37 Å, multiple-scattering from the Oeq atoms to the C1 atoms, multiple-scattering from the Oax atoms, and multiple-scattering between the two nearly linear carbon (C1-C2) atoms. This model is identical to the hydrated uranyl model described above, with the addition of two carbon shells to account for the acetate group attached to the uranyl (Fig. 2A). The importance of the multiple-scattering paths is illustrated by the amplitude ratios in Table 2. If these paths are not included in the model, the χ_γ^2 value increases only slightly because the coordination numbers for the Oeq and C paths increase to unrealistic values to compensate for the loss of amplitude from these important multiple-scattering paths. The data and best-fit model for the aqueous uranyl acetate complex are shown in Figure 3c and d. The model follows the data well over the entire fit range (1.0 to 4.2 Å). The individual contributions for carbon atoms are apparent; the arrows in Figure 3c mark a feature in the uranyl acetate data that is due to the carbon atoms and is not present in the hydrated uranyl data (Fig. 3a).

3.2.3. Aqueous uranyl phosphate

The aqueous uranyl phosphate (U-P) data are shown in Figure 3e and f. The arrows in Figure 3e mark the signals in the Fourier transform due to the phosphorus. Diffraction results (Morosin, 1978; Mercier et al., 1984) for solid uranyl phosphate compounds report U→P distances in the range 3.60 to 3.70 Å. They also report a split in the Oeq shell due to the phosphate. Building on the previously described hydrated uranyl model, we modeled the aqueous uranyl phosphate data with an Oax path, two Oeq paths, multiple-scattering paths from the Oax atoms, a U→P path at approximately 3.6 Å, and a multiple-scattering path U→Oeq→P (Fig. 2B). These paths and their parameterizations are in Table 2. The Oax and corresponding multiple-scattering paths are described in section

3.2.1. The addition of another U→Oeq shell and U→P shell accounts for the phosphate attached to the uranyl. The data and best-fit model are shown in Figure 3e and f. The model follows the data well over the entire fit range (1.1 to 4.0 Å). The arrows in Figure 3e mark the contribution from the P shell that was not needed to describe the hydrated uranyl data (Fig. 3a). The data and fit ranges, along with the goodness-of-fit parameters for this fit, are in Table 1. The significance of the multiple-scattering P paths is illustrated by the amplitude ratios relative to the first oxygen shell (Table 2), and also by the goodness-of-fit values. Including these multiple-scattering paths reduced the χ_γ^2 value by a factor of three.

3.3. U Biomass

The analysis of the hydrated uranyl, aqueous uranyl acetate, and aqueous uranyl phosphate standards described in the previous sections established a qualitative fingerprint for water, acetate, and phosphate groups bound to the uranyl cation. The Fourier transforms of the U biomass data at three different pH values for the lower (U1 series) and higher (Uh series) U concentrations are shown in Figures 4 and 5, respectively. Qualitative observation of these figures indicates that with increasing pH (U11→U12→U13, Uh1→Uh2→Uh3), (1) the signal due to the U→P shell decreases, (2) the signal due to the U→C shell increases, and (3) the signal due to the U→Oeq shell decreases.

The model for the U biomass data combines the paths from the hydrated uranyl, aqueous uranyl acetate, and aqueous uranyl phosphate standards (Table 2). Table 3 summarizes these paths and their parameterization. This model includes two Oax atoms, two shells of equatorial oxygen atoms (Oeq1 and Oeq2), a shell of carbon (C) atoms at approximately 2.85 Å, multiple-scattering paths from the Oeq atoms to the C atom, multiple-scattering paths from the two tightly bound Oax atoms, a shell of phosphorus (P) atoms at approximately 3.74 Å, and multiple-scattering paths from the Oeq atoms to the P atoms. The mean square displacement (σ^2) values for the two Oeq shells were constrained to the same value.

Each data set was tested for the presence of the C and P paths in the fit region (2.0 to 3.8 Å). These tests were performed by fitting each data set with and without the C paths and then again with and without the P paths while simultaneously monitoring the goodness-of-fit parameters. All of the U biomass data needed the contribution from the P paths. For the lowest-pH data, Uh1 and U11, the C path was not needed. The χ_γ^2 value

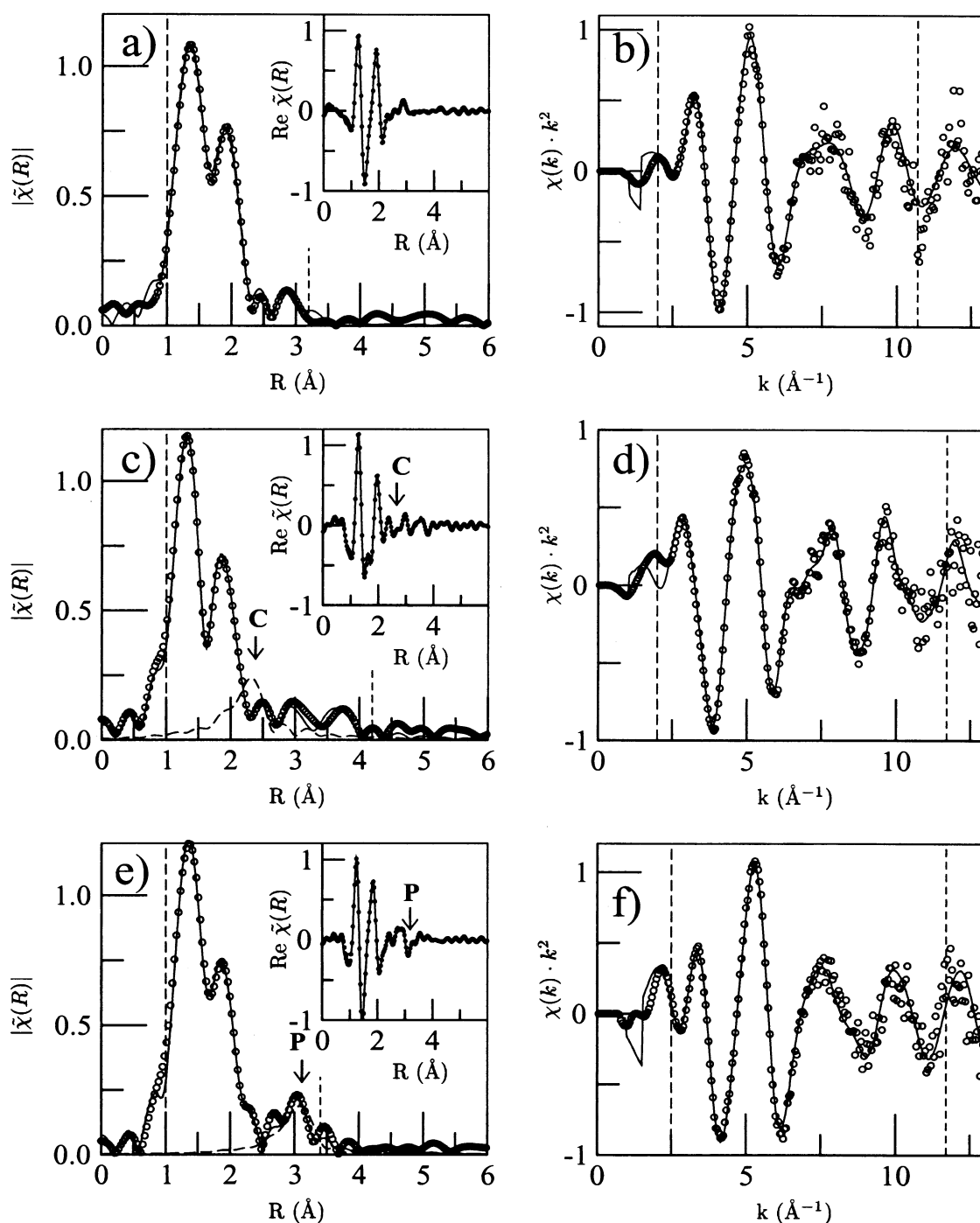


Fig. 3. Data (circles) and best-fit model (line) for the aqueous uranyl standards. (a) Magnitude of Fourier transform, with inset showing real part of Fourier transform for the U-H₂O data. (b) $\chi(k) \times k^2$ for the U-H₂O data. (c) Magnitude of Fourier transform, with inset showing real part of Fourier transform for the U-C data. (d) $\chi(k) \times k^2$ for the U-C data. (e) Magnitude of Fourier transform, with inset showing real part of Fourier transform for the U-P data. (f) $\chi(k) \times k^2$ for the U-P data.

did not change significantly (34 to 29) with a decrease in the degrees of freedom in the fit from 8 to 4 due to the addition of the C paths. Therefore, these paths were not included in the models for lowest-pH data. In contrast, for the higher-pH data, inclusion of the C path was found to be significant, decreasing the χ^2_{ν} value from 58 to 23.

These models were fitted simultaneously to each series of data, U11, U12, and U13 for the low uranyl concentration and Uh1, Uh2, and Uh3 for the high uranyl concentration. The simultaneous fitting was performed in R-space by using k weighting of 1, 2, and 3 for each data set. Therefore, the model was optimized to nine data sets. The data and best-fit model for

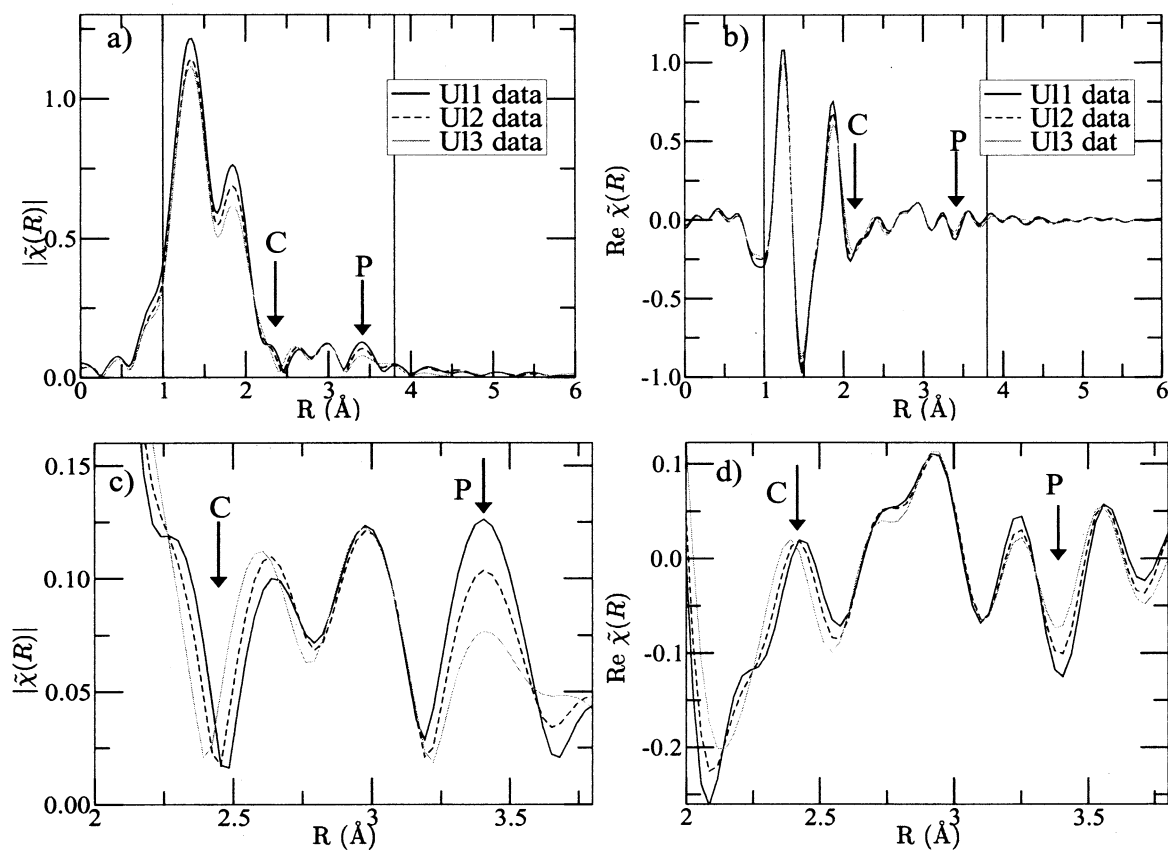


Fig. 4. Comparison of U biomass data U11, U12, and U13. (a) Magnitude of Fourier transform. (b) Real part of Fourier transform. (c) Enlargement of C and P regions in magnitude of Fourier transform. (d) Enlargement of C and P regions in real part of Fourier transform.

the U11 data processed with a k -weighting values of 1, 2, and 3 in the Fourier transform are shown in Figure 6. By use of all three k -weighting values decreases the correlation between the best-fit values for the local atomic uranyl structure, which have different k dependencies. For each series of data, the path length (R_i) values were constrained to a single best-fit value independent of pH. The mean square displacement values were also constrained to a single best-fit value independent of pH, except for the Oeq shell, for which we determined that a pH-dependent σ^2 value was required. The best-fit values for these parameters are listed in Table 4. The data and best-fit model for both the low (U11, U12, and U13) and high (Uh1, Uh2, and Uh3) series, respectively, illustrated with a k weighting of 2 in the Fourier transform, are shown in Figures 7 and 8. The model is in agreement with the data over the entire fit range (1.1 to 3.8 Å) for each pH value.

4. DISCUSSION

4.1. Aqueous Uranyl Standards

4.1.1. Hydrated uranyl

Our XAFS results for the aqueous hydrated uranyl standard are listed in Table 5. The Fourier transform of the data and best-fit model are shown in Figure 3. Our XAFS result for the

Oax distance (1.78 ± 0.01 Å) is similar to the distance reported for other aqueous (1.70 to 1.81 Å) (Antonio et al., 2001) and solid (1.75 to 1.79 Å) (Morosin, 1978; Mercier et al., 1984; Templeton et al., 1985) uranyl compounds. Our XAFS result for the U→Oax σ^2 -value (0.002 ± 0.001 Å²) is similar to values (0.002 to 0.005 Å²) for other aqueous complexes (Allen et al., 1997) and solid (Barger et al., 2000) uranyl compounds. For the uranium to Oeq atoms (U→Oeq), we found a number, distance, and σ^2 value of 6.0 ± 0.4 , 2.42 ± 0.01 Å, and 0.009 ± 0.001 Å², respectively. These values are similar to the number of equatorial waters (4 to 6) (Allen et al., 1997; Thompson et al., 1997; Antonio et al., 2001); the U→Oeq bond lengths (2.41 to 2.43 Å) (Mercier et al., 1984; Allen et al., 1997); and the σ^2 values (0.007 Å²) (Allen et al., 1997) reported previously for U→Oeq of a hydrated uranyl.

4.1.2. Aqueous uranyl acetate

Our XAFS results for the aqueous uranyl acetate standard are in Table 5. The Fourier transform of the data and best-fit model are shown in Figure 3. Our XAFS results for the U→Oax path in the aqueous uranyl acetate standard (bond length 1.78 ± 0.01 Å and mean square displacement 0.001 ± 0.001 Å²) are the same, within the experimental uncertainties, as for the

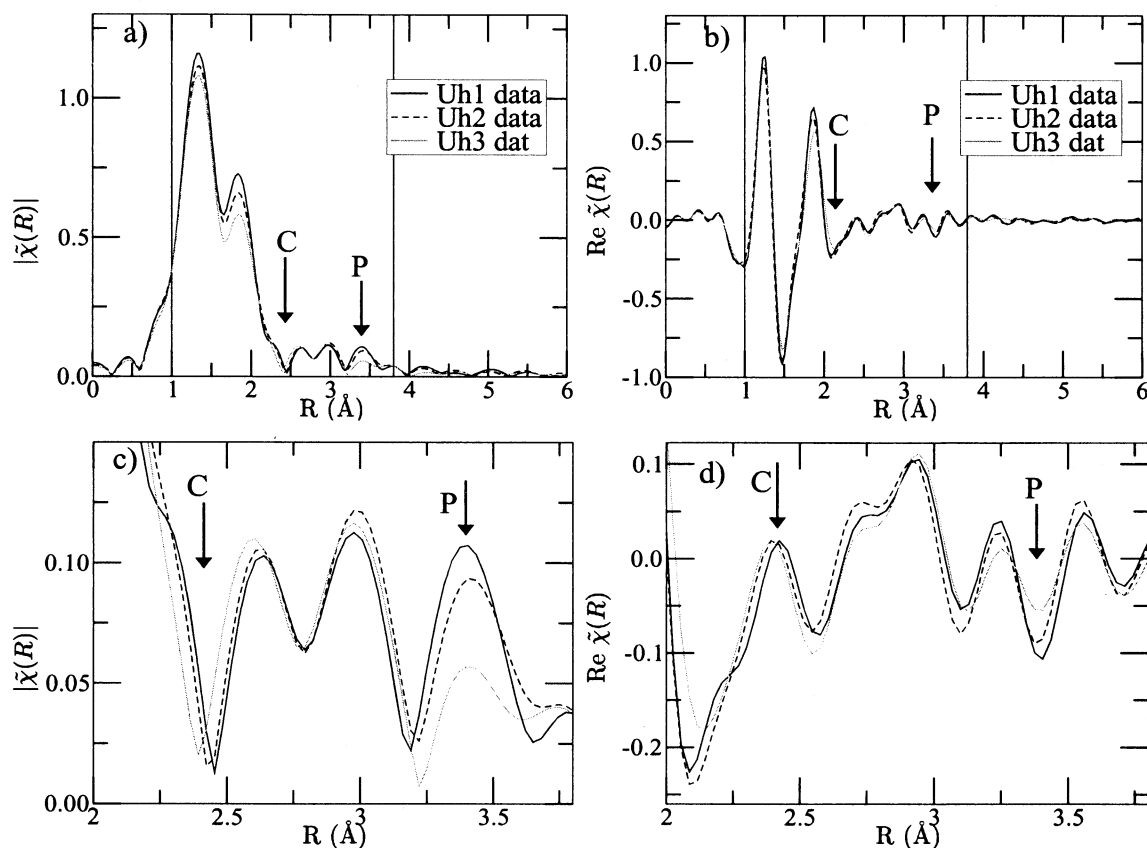


Fig. 5. Comparison of U biomass data Uh1, Uh2, and Uh3. (a) Magnitude of Fourier transform. (b) Real part of Fourier transform. (c) Enlargement of C and P regions in magnitude of Fourier transform. (d) Enlargement of C and P regions in real part of Fourier transform.

hydrated uranyl standard discussed in section 4.1.1. Within the experimental uncertainties, the best-fit values for the $U \rightarrow O_{eq}$ path for the number of O_{eq} atoms (6.0 ± 1.2) and the mean square displacement value ($0.009 \pm 0.002 \text{ \AA}^2$) are the same as the results for the hydrated uranyl standard results discussed in section 4.1.1. The $U-O_{eq}$ bond length has increased from $2.42 \pm 0.01 \text{ \AA}$ for the hydrated uranyl to $2.47 \pm 0.02 \text{ \AA}$ for the aqueous uranyl acetate complex. This bond length ($2.47 \pm 0.02 \text{ \AA}$) compares well with the $U-O_{eq}$ bond length (2.46 \AA) (Allen et al., 1995; Reich et al., 1996) for aqueous $[(UO_2)_3(CO_3)_6]^{6-}$, in which all of the uranyl equatorial oxygen atoms are part of a bidentate carbonate. It is also within the range (2.41 to 2.47 \AA) of bond lengths reported for several types of solid $U-O_{eq}-C$ compounds (Allen et al., 1995; Templeton et al., 1985; Barger et al., 2000). Our XAFS result for the number of carbon (C1) atoms is 3.0 ± 1.5 , indicating that each O_{eq} atom is associated with a carboxyl group (Fig. 2A). The parameterizations listed in Table 2 show that the number of O_{eq} and C1 have not been constrained. On the basis of calculations for aqueous species (section 2.1) the average number of C1 atoms (2.33) is consistent with our XAFS results (3.0 ± 1.5). Our best-fit value for the $U \rightarrow C$ distance ($2.90 \pm 0.02 \text{ \AA}$) and our σ^2 value ($0.003 \pm 0.004 \text{ \AA}^2$) are similar to the values (2.90 \AA and 0.004 \AA^2) (Allen et al., 1995) for aqueous $[(UO_2)_3(CO_3)_6]^{6-}$. Our $U \rightarrow C$ distance ($2.90 \pm 0.02 \text{ \AA}$) is also similar to the previously

reported distances (2.86 to 2.94 \AA) for several chelating (bidentate) solid uranyl-carbon complexes (Howatson et al., 1975; Allen et al., 1995; Barger et al., 2000). Bridging (monodentate) acetate $U \rightarrow C$ distances are longer at 3.98 \AA (Howatson et al., 1975).

4.1.3. Aqueous uranyl phosphate

Our XAFS results for the aqueous uranyl phosphate standard are in Table 5. The Fourier transform of the data and best-fit model are shown in Figure 3. The best-fit values for the two O_{ax} atoms are consistent with those found for the hydrated uranyl standard discussed previously. Our XAFS result for the short O_{eq1} distance of $2.32 \pm 0.02 \text{ \AA}$ compare well with the values (2.31 to 2.35 \AA) reported from diffraction measurements of crystalline structures (Morosin, 1978; Mercier et al., 1984), indicating that we have correctly assigned them to the phosphate groups. Our XAFS results for the longer O_{eq} distance of $2.47 \pm 0.03 \text{ \AA}$ compares well with previously reported values for a hydrated O_{eq} distance (Mercier et al., 1984; Antonio et al., 2001). The σ^2 value for the $U \rightarrow O_{eq}$ path ($0.002 \pm 0.002 \text{ \AA}^2$) is less than the value for the hydrated equatorial uranyl and aqueous uranyl acetate models ($0.009 \pm 0.001 \text{ \AA}^2$). This decrease is due to the removal of a structural σ^2 component included in the single O_{eq} shell model. Constraining our σ^2

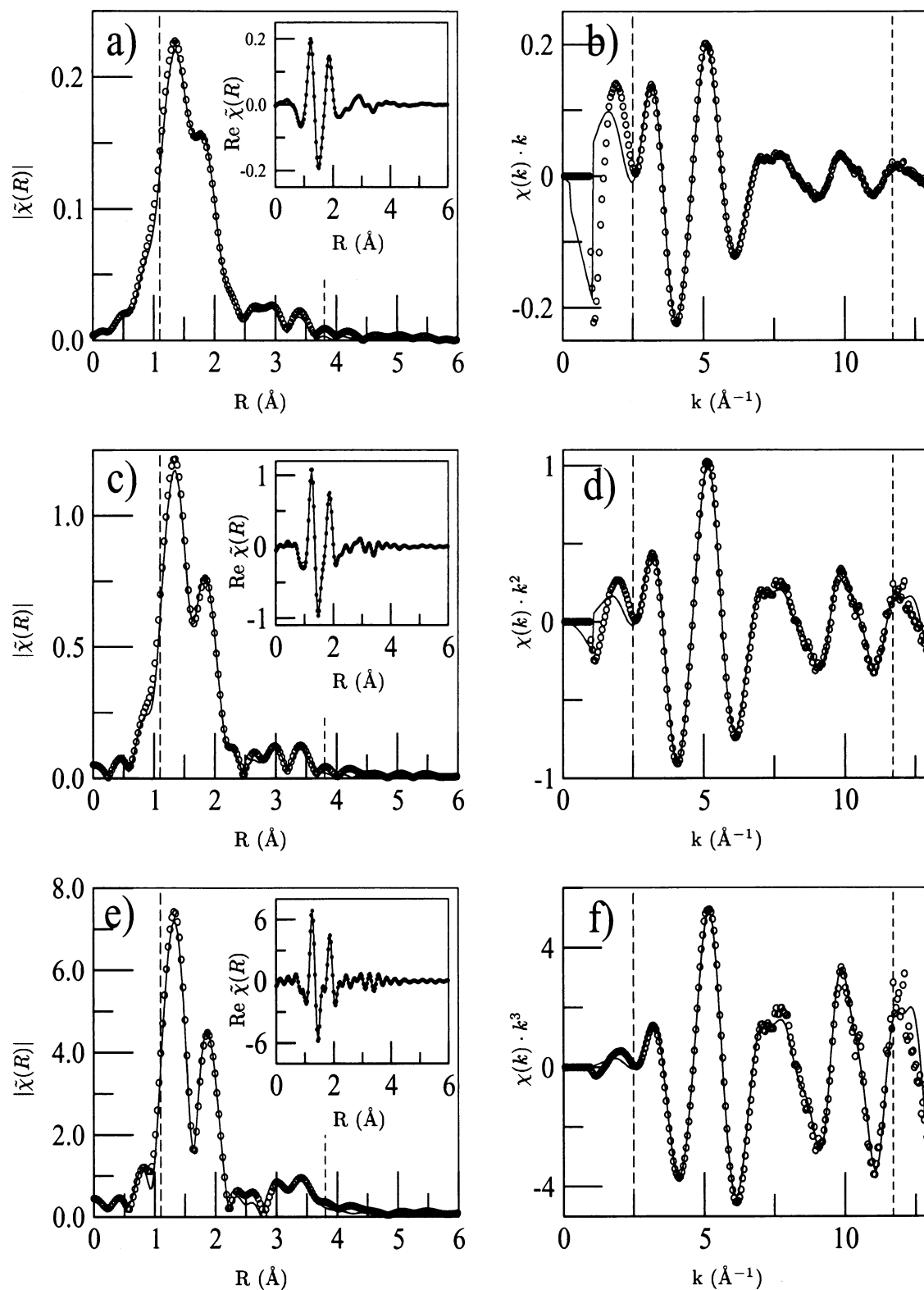


Fig. 6. Data (circles) and best-fit model (line) for U biomass data, U11. (a) Magnitude of Fourier transform, with real part of Fourier transform processed with a k weighting of 1 (inset). (b) $\chi(k) \times k^1$. (c) Magnitude of Fourier transform, with real part of Fourier transform processed with a k weighting of 2 (inset). (d) $\chi(k) \times k^2$. (e) Magnitude of Fourier transform, with real part of Fourier transform processed with a k weighting of 3 (inset). (f) $\chi(k) \times k^3$.

Table 4. Best-fit values for the pH-independent parameters for local structure about uranium sorbed to biomass.

Path	N_{degen}	R (Å)	σ^2 (10^{-3} Å ²)	E_0 (eV)
			UI1, UI2, UI3	
U→Oax	2.0 ^a	1.77 ± 0.01	2 ± 1	0.2 ± 0.9
U→Oeq1	N_2	2.33 ± 0.02	4, 7, 10 ± 3	4.4 ± 1.1
U→Oeq2	N_3	2.45 ± 0.02	4, 7, 10 ± 3	4.4 ± 1.1
U→C	N_4	2.89 ± 0.02	1 ± 5	4.4 ± 1.1
U→Oeq→C	4 × N_4	3.32 ± 0.02	1 ± 5	4.4 ± 1.1
U→Oax1→U→Oax1	2.0 ^a	3.53 ± 0.01	3 ± 1	0.2 ± 0.9
U→Oax1→Oax2	2.0 ^a	3.53 ± 0.01	3 ± 1	0.2 ± 0.9
U→Oax1→U→Oax2	2.0 ^a	3.53 ± 0.01	3 ± 1	0.2 ± 0.9
U→P	N_6	3.64 ± 0.01	3 ± 3	4.4 ± 1.1
U→Oeq1→P	2 × N_6	3.78 ± 0.01	3 ± 3	4.4 ± 1.1
			Uh1, Uh2, Uh3	
U→Oax	2.0 ^a	1.76 ± 0.01	2 ± 1	1.0 ± 0.7
U→Oeq1	N_2	2.32 ± 0.02	4, 6, 9 ± 2	5.2 ± 0.9
U→Oeq2	N_3	2.45 ± 0.02	4, 6, 9 ± 2	5.2 ± 0.9
U→C	N_4	2.89 ± 0.02	2 ± 4	5.2 ± 0.9
U→Oeq→C	4 × N_4	3.33 ± 0.02	2 ± 4	5.2 ± 0.9
U→Oax1→U→Oax1	2.0 ^a	3.53 ± 0.01	4 ± 1	1.0 ± 0.7
U→Oax1→Oax2	2.0 ^a	3.53 ± 0.01	4 ± 1	1.0 ± 0.7
U→Oax1→U→Oax2	2.0 ^a	3.53 ± 0.01	4 ± 1	1.0 ± 0.7
U→P	N_6	3.64 ± 0.01	2 ± 3	5.2 ± 0.9
U→Oeq1→P	2 × N_6	3.77 ± 0.01	2 ± 3	5.2 ± 0.9

^a Values without uncertainties were held constant during the fit.

values to 0.01 Å², as has been done in earlier work (Barger et al., 2000), results in an overestimation of the number of Oeq atoms in our system. For our XAFS data, the amount of overestimation corresponds to ~40% for Oeq shells. On the basis of calculations for aqueous species (see section 2.1), the average number of P atoms (1.42) is consistent with our XAFS results (1.0 ± 0.8). The P distance of 3.64 ± 0.04 Å, consistent with the range of previously reported values (3.60 to 3.70 Å) (Morosin, 1978; Mercier et al., 1984) for solid inorganic compounds, indicates monodentate phosphate binding (Fig. 2B).

4.2. U Biomass

In most cases, the best-fit values for both the UI and Uh series are consistent with each other. Therefore, only the values for the Uh series are quoted in the text. If differences were significant, both results are discussed. Our XAFS result (Table 4) for the Oax distance (1.76 ± 0.01 Å) is similar to the distance found for the uranyl standards (1.77 to 1.78 ± 0.01 Å). The short equatorial oxygen (U-Oeq1) bond length (2.32 ± 0.02 Å) is the same as the distance found for the aqueous uranyl phosphate standard (2.32 ± 0.02 Å) and is within the range of previously reported values for the oxygen atom of the phosphate bound to a uranyl (2.24 to 2.35 Å) (Morosin, 1978; Mercier et al., 1984). The longer equatorial oxygen (U-Oeq2) bond length (2.45 ± 0.02 Å) is consistent with the distance found for the aqueous uranyl phosphate standard (2.47 ± 0.03 Å) and similar to previously reported values for the oxygen atom of the carboxyl or water bound to a uranyl (2.41 to 2.51 Å) (Howatson et al., 1975; Allen et al., 1995; Barger et al., 2000). The best-fit value for the U→C path length ($r = 2.89 ± 0.02$ Å) is consistent with the aqueous uranyl acetate standard (2.90 ± 0.02 Å) and similar to previously reported values for acetate bound to uranyl. The phosphorus (P) distance (3.64 ± 0.01 Å) is the same as that found for the aqueous uranyl

phosphate standard (3.64 ± 0.01 Å) and within the range of previously reported values for a phosphate bound to a uranyl in a crystal structure (3.60 to 3.70 Å) (Morosin, 1978; Mercier et al., 1984).

Our XAFS result (Table 4) for the U→Oax σ^2 -value (0.002 ± 0.001 Å²) is consistent with the value found for the uranyl standards (0.001 to 0.002 ± 0.001 Å²). These values compare well with reported values discussed in section 3.2.1. The σ^2 values for the equatorial oxygen shells increase with pH (0.004, 0.006, 0.009 ± 0.002 Å²) and are consistent with the range of values for the aqueous uranyl standards (0.002 to 0.009 ± 0.002 Å²). The best-fit value for the U→C mean square displacement ($\sigma^2 = 0.002 ± 0.004$ Å²) is similar to the value for the aqueous uranyl acetate standard (0.003 ± 0.004 Å²). The σ^2 value for the U→P paths (0.002 ± 0.003 Å²) is similar to the value for the aqueous uranyl phosphate standard (0.008 ± 0.005 Å²).

The pH dependence for the number of equatorial oxygen, carbon, and phosphorus atoms is summarized in Table 6. The number of P atoms decreases slightly as the pH increases. The high correlations in the numbers of P and C atoms, the values for their distances from the uranyl, and their mean-square displacement values make the uncertainties in the numbers of P and C atoms large. For the high uranyl:biomass ratio, the number of phosphoryl bonds (P atoms) decreases from 1.9 ± 0.9 to 0.8 ± 0.5 as the pH increases from 1.67 to 4.80. The results are similar for the low uranyl:biomass ratio. For the high uranyl:biomass ratio, the number of carboxyl bonds (carbon atoms) is consistent with zero at pH 1.67, and the number increases to nonzero values (0.5 ± 0.4 and 1.0 ± 0.7) at the higher pH values (3.22 and 4.80, respectively). The results are similar for the low uranium:biomass ratio.

On the basis of previous studies, a uranyl to carbon distance of approximately 2.90 Å indicates a bidentate carboxyl bond

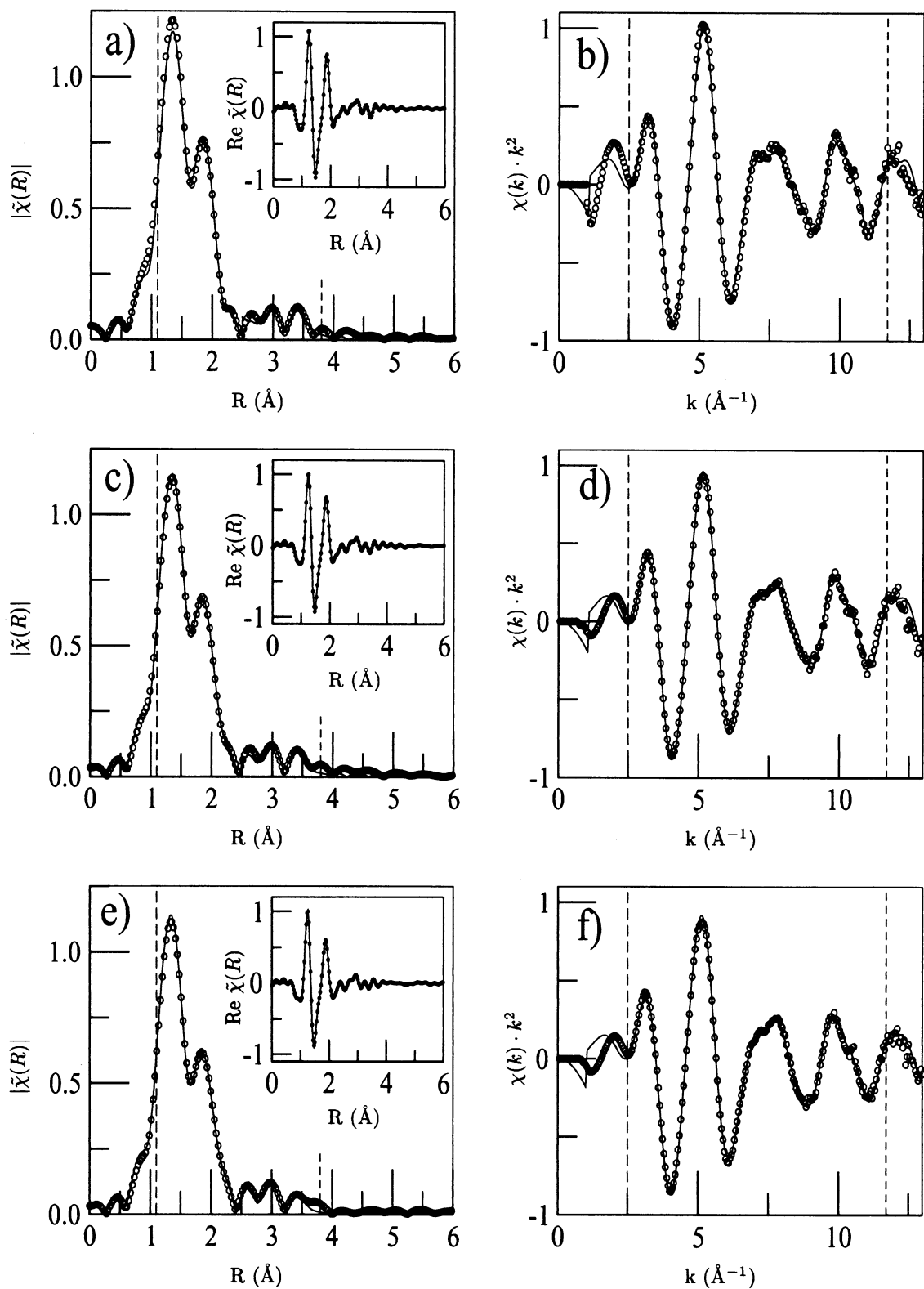


Fig. 7. Data (circles) and best-fit model (line) for U biomass data, U11, U12, and U13. (a) Magnitude of Fourier transform, with real part of Fourier transform of U11 (inset). (b) $\chi(k) \times k^2$ of U11. (c) Magnitude of Fourier transform, with real part of Fourier transform of U12 (inset). (d) $\chi(k) \times k^2$ of U12. (e) Magnitude of Fourier transform, with real part of Fourier transform of U13 (inset). (f) $\chi(k) \times k^2$ of U13.

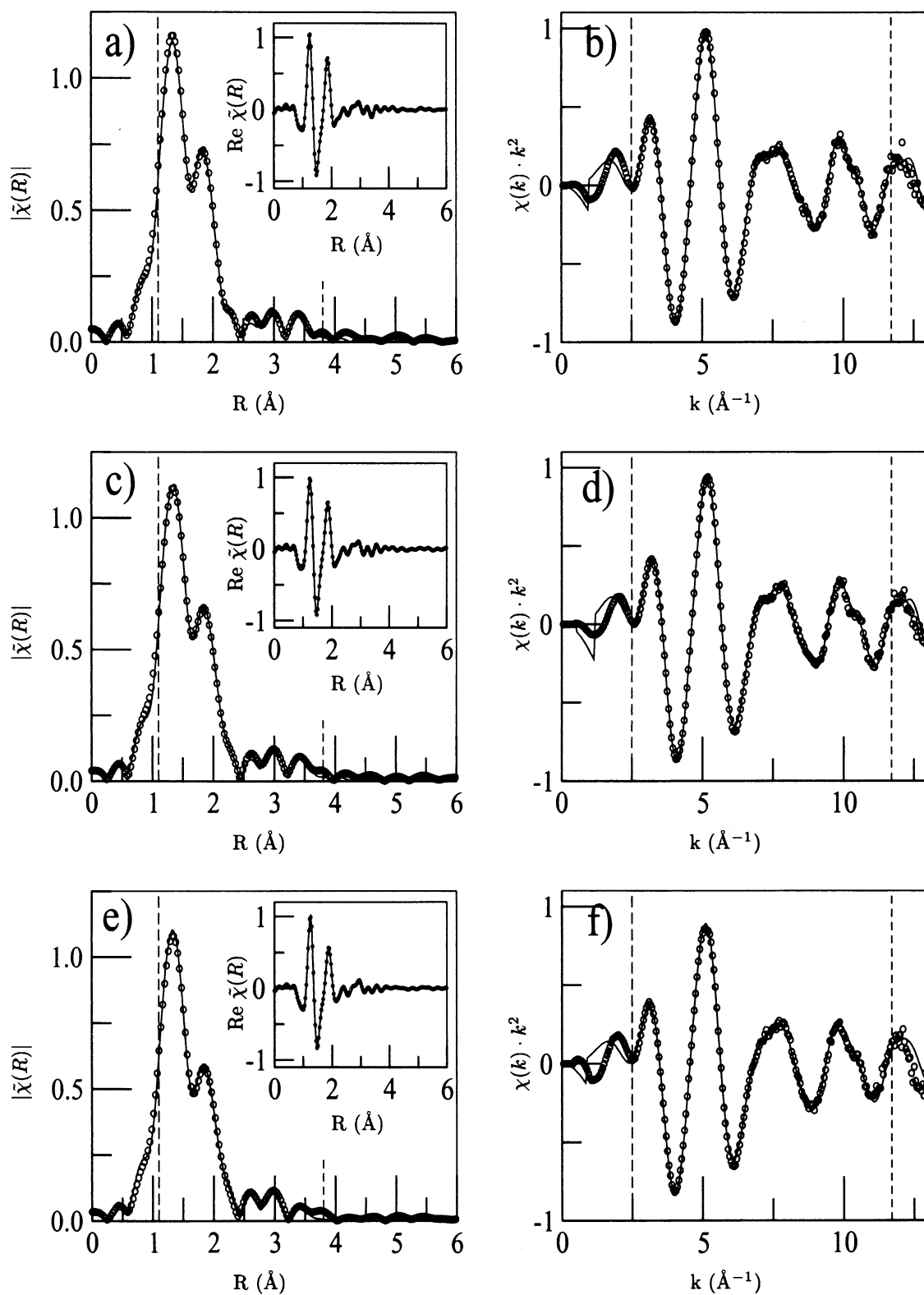


Fig. 8. Data (circles) and best-fit model (line) for U biomass data, Uh1, Uh2, and Uh3. (a) Magnitude of Fourier transform, with real part of Fourier transform of Uh1 (inset). (b) $\chi(k) \times k^2$ of Uh1. (c) Magnitude of Fourier transform, with real part of Fourier transform of Uh2 (inset). (d) $\chi(k) \times k^2$ of Uh2. (e) Magnitude of Fourier transform, with real part of Fourier transform of Uh3 (inset). (f) $\chi(k) \times k^2$ of Uh3.

Table 5. Best-fit values for hydrated uranyl (U-H₂O), uranyl acetate (U-C), and uranyl phosphate (U-P) standards.^a

Path	N _{degen}	R (Å)	σ ² (10 ⁻³ Å ²)	E ₀ (eV)
U-H ₂ O				
U→Oax	2.0 ^b	1.78 ± 0.01	2 ± 1	4.1 ± 0.9
U→Oeq	6.0 ± 0.4	2.42 ± 0.01	9 ± 1	7.6 ± 0.7
U→Oax1→U→Oax1	2.0 ^b	3.56 ± 0.01	3 ± 1	4.1 ± 0.9
U→Oax1→Oax2	2.0 ^b	3.56 ± 0.01	3 ± 1	4.1 ± 0.9
U→Oax1→U→Oax2	2.0 ^b	3.56 ± 0.01	3 ± 1	4.1 ± 0.9
U-C				
U→Oax	2.0 ^b	1.78 ± 0.01	1 ± 1	-1.6 ± 1.4
U→Oeq	6.8 ± 1.2	2.47 ± 0.02	9 ± 2	3.8 ± 1.2
U→C1	3.0 ± 1.5	2.90 ± 0.02	3 ± 4	5.1 ± 1.5
U→Oeq→C1	12.0 ± 6.0	3.26 ± 0.06	3 ± 4	4.5 ± 1.0
U→Oax1→U→Oax1	2.0 ^b	3.56 ± 0.01	2 ± 1	-1.6 ± 1.4
U→Oax1→Oax2	2.0 ^b	3.56 ± 0.01	2 ± 1	-1.6 ± 1.4
U→Oax1→U→Oax2→U	2.0 ^b	3.56 ± 0.01	2 ± 1	-1.6 ± 1.4
U→C2	3.0 ± 1.5	4.37 ± 0.05	5 ± 5	5.1 ± 1.5
U→C1→C2	6.0 ± 1.5	4.37 ± 0.05	5 ± 5	5.1 ± 1.5
U-P				
U→Oax	2.0 ^b	1.77 ± 0.01	1 ± 1	3.7 ± 1.3
U→Oeq1	2.9 ± 0.6	2.32 ± 0.02	2 ± 2	9.0 ± 1.0
U→Oeq2	2.4 ± 0.4	2.47 ± 0.03	2 ± 2	9.0 ± 1.0
U→Oax1→Oax2	2.0 ^b	3.53 ± 0.02	1 ± 1	3.7 ± 1.3
U→Oax1→U→Oax2	2.0 ^b	3.53 ± 0.02	1 ± 1	3.7 ± 1.3
U→Oax1→U→Oax1	2.0 ^b	3.53 ± 0.02	1 ± 1	3.7 ± 1.3
U→P	1.0 ± 0.8	3.64 ± 0.04	8 ± 5	9.0 ± 1.0
U→Oeq1→P	2.0 ± 1.6	3.76 ± 0.04	8 ± 5	9.0 ± 1.0

^a S₀² was found to converge to 1.0 ± 0.10 for all U L3 XAFS measurements.

^b Values without uncertainties were not determined in the fit but were held at the given value.

(Howatson et al., 1975; Templeton et al., 1985). In this study, bidentate refers to an inner-sphere complex where two oxygen atoms of a single carboxyl functional group are shared with the uranyl, rather than oxygen atoms of two carboxyl groups (Fig. 2A). Therefore, there should be at least two longer equatorial oxygen (Oeq2) bonds for every carbon atom, and there could be more Oeq2 atoms because of water bound to the uranyl. As Table 6 shows, the best-fit value for number of Oeq2 atoms (2.4 to 2.7 to 3.3) is more than twice number of C atoms (0 to 0.5 to 1.0) for the high uranyl:biomass ratio. Again the results are similar for the low uranyl:biomass ratio.

The amount of uranium that is adsorbed to the biomass is not

constant with pH. At low pH, all cell wall functional groups are protonated, and therefore less adsorption occurs. As the functional groups become deprotonated with increasing pH, the electronegativity of the cell wall increases, causing adsorption to increase. This trend is important in interpreting the average numbers of phosphoryl and carboxyl ligands attached to the uranyl. At pH 1.67, we observe only phosphoryl binding. With increasing pH above 1.67, we detect not only the onset of carboxyl binding, but also an increase in the total number of uranyl atoms bound to the cell walls. The slight decrease in the number of phosphoryl groups bound to the uranyl atom with increasing pH could be due to two factors: (1) the uranyl is

Table 6. The pH dependence for the number of Oeq1, Oeq2, C, and P atoms and their distance from the uranium atom.

Atom type	R (Å)	No. of neighboring atoms		
		U11 (pH = 1.67)	U12 (pH = 3.22)	U13 (pH = 4.80)
Oax	1.77 ± 0.01	2.0 ^a	2.0 ^a	2.0 ^a
Oeq1	2.33 ± 0.03	3.1 ± 0.8	3.1 ± 0.9	2.9 ± 0.8
Oeq2	2.45 ± 0.03	2.3 ± 0.7	2.7 ± 0.8	3.3 ± 1.0
C	2.89 ± 0.02	~0 ^b	0.4 ± 0.4	0.9 ± 0.7
P	3.64 ± 0.01	2.4 ± 1.3	1.9 ± 1.1	1.3 ± 0.8
		Uh1 (pH = 1.67)	Uh2 (pH = 3.22)	Uh3 (pH = 4.80)
Oax	1.76 ± 0.01	2.0 ^a	2.0 ^a	2.0 ^a
Oeq1	2.32 ± 0.02	2.9 ± 0.5	2.8 ± 0.5	2.8 ± 0.5
Oeq2	2.45 ± 0.02	2.4 ± 0.4	2.7 ± 0.4	3.3 ± 0.6
C	2.89 ± 0.02	~0 ^b	0.5 ± 0.4	1.0 ± 0.7
P	3.64 ± 0.01	1.9 ± 0.9	1.7 ± 0.8	0.8 ± 0.5

^a The number of Oax atoms was held at 2.0.

^b The carbon atom was not included in the fit for the lowest-pH data.

preferentially adsorbed to the carboxyl ligand relative to the protonated phosphoryl site (so that as the carboxyl becomes deprotonated, carboxyl binding replaces phosphoryl binding to some extent with increasing pH) and/or (2) the number of uranyl atoms bound to the phosphoryl group is constant, and additional uranium is bound to the carboxyl group. Both of these situations would result in a decrease in the average number of phosphoryl groups bound to the uranyl atom, and they cannot be distinguished on the basis of the XAFS data alone.

Fowle et al. (2000) measured the extent of uranyl adsorption to suspensions of *B. subtilis* in 0.1 mol/L NaClO₄ as a function of pH. They observed significant amounts of uranyl adsorption below pH 2.5, with no pH dependence for this adsorption at least down to pH 1.5. This extent of pH-independent bacterial adsorption at low pH was not observed for any other aqueous cations studied (Fein et al., 1997). Above pH 2.5, Fowle et al. (2000) observed an increase in the extent of adsorption with increasing pH, behavior typical of other cations in this pH range. On the basis of these indirect observations, Fowle et al. (2000) postulated that the low-pH adsorption was caused by uranyl binding with protonated phosphoryl groups on the cell wall, whereas the behavior at higher pH was caused by uranyl binding with bacterial carboxyl groups. Thermodynamic stability constants were determined for each type of bacterial surface complex. The pH-independent adsorption behavior would be expected at low pH, because the concentration of protonated phosphoryl sites does not change markedly until the pH approaches the pK_a of the phosphoryl sites (6.9). Carboxyl sites, with a pK_a of 4.8, deprotonate at lower pH, and therefore uranyl binding to these sites increases with increasing pH above pH 2.5.

The XAFS data from this study are completely independent from the adsorption data set of Fowle et al. (2000), yet they offer identical conclusions regarding the nature of uranyl binding to the cell wall of *B. subtilis*. The XAFS data demonstrate that low-pH binding is caused by a phosphoryl site, and increased binding to carboxyl sites is observed as an increase in adsorption with increasing pH above pH 2.5. Fein et al. (1997) identified the cell wall sites with a pK_a value of 4.8 as being carboxyl, entirely on the basis of similar typical pK_a values of carboxyl functional groups for aqueous organic acid molecules. This study provides direct confirmation of the importance of carboxyl binding sites in this pH range. This study also demonstrates the power of incorporating spectroscopic measurements with bulk adsorption measurements to yield both detailed constraints on the nature and stoichiometry of the important binding reactions and thermodynamic properties of surface species.

5. CONCLUSIONS

The uranium L3-edge XANES measurements of the U biomass data and U(IV) and U(VI) standards clearly indicate that U(VI) added to biomass samples was not reduced by either the bacteria or radiation exposure during XAFS measurements. The uranium L3-edge XAFS data give information about the average local atomic environment of the U atoms in the biomass samples. The Fourier transforms of the XAFS data at three different pH values (1.67, 3.22, and 4.80) and two dif-

ferent U:bacteria concentration ratios show changes in the uranyl local atomic environment due to different percentages of phosphoryl and/or carboxyl groups bound to the uranyl ion. At the lowest pH value (1.67) and at both U:bacteria ratios (U11 and Uh1), the XAFS data indicate uranyl binding to a phosphoryl functional group, with an average distance between the uranium atom and the phosphorus atom of approximately 3.6 Å. This distance is indicative of an inner-sphere complex with one oxygen atom shared between the uranyl and the phosphoryl ligand (Fig. 2B). No carboxyl-uranyl bonds are needed to model the XAFS data accurately for the low-pH samples (U11 and Uh1). Our detection limit for the number of carbon atoms is 0.2 because of interference in the data from equatorial oxygen atoms. Therefore, we cannot completely rule out the possibility of a small carboxyl component at pH 1.67. At the higher pH values (3.22 and 4.80), inclusion of C atoms is required to accurately simulate the experimental data (U12, U13, Uh2, and Uh3). The C atom distance of approximately 2.9 Å indicates that the uranyl-carboxyl bond is also the inner-sphere type, with two oxygen atoms shared between the uranyl and the carboxyl ligand (Fig. 2A). These results indicate an increase in the number of carboxyl bonds with increasing pH (Table 6). Our XAFS results are consistent with the surface complexation models proposed by Fein et al. (1997) and Fowle et al. (2000), demonstrating the complementary role XAFS spectroscopy and bulk adsorption measurements can play in determining metal distribution behaviors in the environment.

Acknowledgments—Special appreciation is extended to E. J. O'Loughlin for insightful discussions and assistance with U XAFS data collection and also to P. C. Burns and A. J. Locoek for additional insightful discussions and for the U(VI) and U(IV) standards. N. Leyarovska is acknowledged for her assistance with U XAFS data collection at the MRCAT sector. We thank P. A. O'Day and three anonymous reviewers for their constructive comments. Support for S.D.K. and K.M.K. was provided by the U.S. Department of Energy, Office of Science, Office of Biologic and Environmental Research, NABIR Program. This research was also supported in part by the U.S. National Science Foundation (grant EAR-9905704) and by the Donors of the Petroleum Research Fund, administered by the American Chemical Society. Use of the MR-CAT sector at the Advanced Photon Source (APS) and of the APS was supported by the U.S. Department of Energy, Office of Science, Office of Basic Energy Sciences, under contract W-31-109-ENG-38.

Associate editor: P. A. O'Day

REFERENCES

- Allen P. G., Bucher J. J., Clark D. L., Edelstein N. M., Ekberg S. A., Gohdes J. W., Hudson E. A., Kaltsoyannis N., Lukens W. W., Neu M. P., Palmer P. D., Reich T., Shuh D. K., Tait C. D., and Zwick B. D. (1995) Multinuclear NMR, Raman, EXAFS, and X-ray diffraction studies of uranyl carbonate complexes in near-neutral aqueous solution: X-ray structure of [C(NH₂)₃]₆[(UO₂)₃(CO₃)₆].6.5H₂O. *Inorg. Chem.* **34**, 4797–4807.
- Allen P. G., Shuh D. K., Bucher J. J., Edelstein N. M., Reich T., Denecke M. A., and Nitsche H. (1996) EXAFS determination of uranium structures: The uranyl ion complexed with tartaric, citric, and malic acids. *Inorg. Chem.* **35**, 784–787.
- Allen P. G., Bucher J. J., Sheh D. K., Edelstein N. M., and Reich T. (1997) Investigation of aquo and chloro complexes of UO₂²⁺, NpO₂²⁺, Np⁴⁺, and Pu³⁺ by X-ray absorption fine structure spectroscopy. *Inorg. Chem.* **36**, 4676–4683.

- Antonio M. R., Soderholm L., Williams C. W., Blaudeau J. P., and Bursten B. E. (2001) Neptunium redox speciation. *Radiochim. Acta* **89**, 17–25.
- Barger J. R., Reitmeyer R., Lenhart J. J., and Davis J. A. (2000) Characterization of U(VI)-carbonate ternary complexes on hematite: EXAFS and electrophoretic mobility measurements. *Geochim. Cosmochim. Acta* **64**, 2737–2749.
- Beolchini F., Pagnanelli F., and Veglio F. (2001) Modeling of copper biosorption by *Arthrobacter* sp. in a UF/MF membrane reactor. *Environ. Sci. Technol.* **35**, 3048–3054.
- Bethke C. M. and Brady P. V. (2000) How the K-d approach undermines ground water cleanup. *Ground Water* **38**, 435–443.
- Beveridge T. J. and Murray R. G. E. (1976) Uptake and retention of metals by cell walls of *Bacillus subtilis*. *J. Bacteriol.* **127**, 1502–1518.
- Beveridge T. J. and Murray R. G. E. (1980) Sites of metal deposition in the cell wall of *Bacillus subtilis*. *J. Bacteriol.* **141**, 876–887.
- Cox J. S., Smith D. S., Warren L. A., and Ferris F. G. (1999) Characterizing heterogeneous bacterial surface functional groups using discrete affinity spectra for proton binding. *Environ. Sci. Technol.* **33**, 4514–4521.
- Cross J. L. and Frenkel A. I. (1998) Use of scattered radiation for absolute energy calibration. *Rev. Sci. Instrum.* **70**, 38–40.
- Daughney C. J., Fein J. B., and Yee N. (1998) A comparison of the thermodynamics of metal adsorption onto two gram-positive bacteria. *Chem. Geol.* **144**, 161–176.
- Dent A. J., Ramsay J. D. F., and Swanton S. W. (1992) An EXAFS study of uranyl ion in solution and sorbed onto silica and montmorillonite clay colloids. *J. Colloid Interface Sci.* **150**, 45–60.
- Docrat T. L., Mosselmans J. F. W., Charnock J. M., Whiteley M. W., Collison D., Livens F. R., Jones C., and Edmiston M. J. (1999) X-ray absorption spectroscopy of tricarbonatodioxouranate(V), $[\text{UO}_2(\text{CO}_3)_3]^{5-}$, in aqueous solution. *Inorg. Chem.* **38**, 1879–1882.
- Duff M. C., Morris D. E., Hunter D. B., and Bertsch P. M. (2000) Spectroscopic characterization of uranium in evaporation basin sediments. *Geochim. Cosmochim. Acta* **64**, 1535–1550.
- Fein J. B., Daughney C. J., Yee N., and Davis T. A. (1997) A chemical equilibrium model for metal adsorption onto bacterial surface. *Geochim. Cosmochim. Acta* **61**, 3319–3328.
- Fein J. B. and Delea D. (1999) Experimental study of the effect of EDTA on Cd adsorption by *Bacillus subtilis*. **161**, 375–383.
- Ferris F. G., Schultze S., Witten T. C., Fyfe W. S., and Beveridge T. J. (1989) Metal interactions with microbial biofilms in acidic and neutral pH environments. *Appl. Environ. Microbiol.* **55**, 1249–1257.
- Fowle D. A. and Fein J. B. (1999) Competitive adsorption of metal cations onto two gram positive bacteria: Testing the chemical equilibrium model. *Geochim. Cosmochim. Acta* **63**, 3059–3067.
- Fowle D. A., Fein J. B., and Martin A. M. (2000) Experimental study of uranyl adsorption onto *Bacillus subtilis*. *Environ. Sci. Technol.* **34**, 3737–3741.
- Francis A. J., Gillow J. B., Dodge C. J., Dunn M., Mantione K., Strietelmeier B. A., Pansoy-Hjelvik M. E., and Papenguth H. W. (1998) Role of bacteria as biocolloids in the transport of actinides from a deep underground radioactive waste repository. *Radiochim. Acta* **82**, 347–354.
- Gonçalves M. L. S., Sigg L., Reutlinger M., and Stumm W. (1987) Metal ion binding by biological surfaces: Voltammetric assessment in the presence of bacteria. *Sci. Total Environ.* **60**, 105–119.
- Grenthe I., Fuger J., Konings R. J. M., Lemire R. J., Muler A. B. (1992) *Chemical Thermodynamics of Uranium*. Elsevier.
- Harden V. P. and Harris J. O. (1953) The isoelectric point of bacterial cells. *J. Bacteriol.* **65**, 198–202.
- Harvey R. W. and Leckie J. O. (1985) Sorption of lead onto two gram-negative marine bacteria in seawater. *Mar. Chem.* **15**, 333–344.
- Harvey R. W., Lion L. W., Young L. Y., and Leckie J. O. (1982) Enrichment and association of lead and bacteria at particulate surfaces in a salt-march surface layer. *J. Mar. Res.* **40**, 1201–1211.
- Hay P. J., Martin R. L., and Schreckenbach G. (2000) Theoretical studies of the properties and solution chemistry of AnO_2^{2+} and AnO_2^+ aquo complexes for An = U, Np, and Pu. *J. Phys. Chem. A* **104**, 6259–6270.
- He L. M. and Tebo B. M. (1998) Surface charge properties of and Cu(II) adsorption by spores of the marine *Bacillus* sp. strain SG-1. **64**, 1123–1129.
- Hennig C., Panak P. J., Reich T., Raff J., Selenska-Poball S., Bernhard G., and Nitsche H. (2000) Uranium(VI) complexation by *Bacillus* species isolated from uranium mining waste pile—A comparative EXAFS study. In *Programme and Abstracts of the 2nd Euroconference on Bacteria-Metal/Radionuclide Interaction: Basic Research and Bioremediation*. Rossendorf.
- Howatson J., Grev D. M., and Morosin B. (1975) Crystal and molecular structure of uranyl acetate dihydrate. *J. Inorg. Nucl. Chem.* **37**, 1933–1935.
- Hudson E. A., Rehr J. J., and Bucher J. J. (1995) Multiple-scattering calculations of the uranium L3-edge X-ray-absorption near-edge structure. *Phys. Rev. B* **52**, 13815–3826.
- Kemner K. M., Kropf A. J., and Bunker B. A. (1994) A low-temperature total electron yield detector for X-ray absorption fine structure spectra. *Rev. Sci. Instrum.* **65**, 3667–3669.
- Konhauser K., Fyfe W. S., and Ferris F. G. (1993) Metal sorption and mineral precipitation by bacteria in 2 Amazonian river systems, Rio-Solimoes and Rio-Negro, Brazil. *Geology* **21**, 1103–1106.
- Koretsky C. (2000) The significance of surface complexation reactions in hydrologic systems: A geochemist's perspective. *J. Hydrol.* **230**, 127–171.
- Ledin M., Krantz-Rulcker C., and Allard B. (1999) Microorganisms as metal sorbents: Comparison with other soil constituents in multi-compartment systems. *Soil. Biol. Biochem.* **31**, 1639–1648.
- Mercier R., Pham Thi M., and Colomban P. (1984) Structure, vibrational study and conductivity of the trihydrated uranyl bis(dihydrogenophosphate): $\text{UO}_2(\text{H}_2\text{PO}_4)_2 \cdot 3\text{H}_2\text{O}$. *Solid State Ionics* **15**, 113–126.
- Morosin B. (1978) Hydrogen uranyl phosphate tetrahydrate, a hydrogen ion solid electrolyte. *Acta Cryst.* **B34**, 3732–3734.
- Morris D. E., Allen P. G., Berg J. M., Chisholm-Brause C. J., Conradson S. D., Donohoe R. J., Hess N. J., Musgrave J. A., and Tait C. D. (1996) Speciation of uranium in Fernald soils by molecular spectroscopic methods: Characterization of untreated soils. *Environ. Sci. Technol.* **30**, 2322–2331.
- Mullen M. D., Wolf B. C., Ferris F. G., Beveridge T. J., Flemming C. A., and Bailey G. W. (1989) Bacterial sorption of heavy metals. *Appl. Environ. Microbiol.* **55**, 3300–3306.
- Newville M., Livinš P., Yacoby Y., Rehr J. J., and Stern E. A. (1993) Near-edge X-ray absorption fine structure of Pb: A comparison of theory and experiment. *Phys. Rev. B* **47**, 14126–14131.
- Newville M., Ravel B., Haskel D., and Stern E. A. (1995) Analysis of multiple scattering XAFS data using theoretical standards. *Physica B* **208/209**, 154–156.
- Norber A. B. and Persson H. (1984) Accumulation of heavy-metal ions by *Zoogloea ramigera*. *Biotechnol. Bioengineer.* **26**, 239–246.
- Plette A. C. C., van Riemsdijk W. H., Benedetti M. F., and Van der Wal A. (1995) pH dependent charging behavior of isolated cell walls of a gram-positive soil bacterium. *J. Colloid Interface Sci.* **173**, 354–363.
- Reeder R. J., Nugent M., Lamble G. M., Tait C. D., and Morris D. E. (2000) Uranyl incorporation into calcite and aragonite: XAFS and luminescence studies. *Environ. Sci. Technol.* **34**, 638–644.
- Reich T., Denecke M. A., Pompe S., Bubner M., Heise K.-H., Schmidt M., Brendler V., Baraniak L., Nitsche H., Allen P. G., Bucher J. J., Edelstein N. M., and Shuh D. K. (1996) Characterization of the interaction of uranyl ions with humic acids by X-ray absorption spectroscopy. In *Synchrotron Radiation Techniques in Industrial, Chemical, and Material Science* (ed. D'Amico). Plenum Press.
- Sarret G., Manceau A., Spadini L., Roux J.-C., Hazemann J.-L., Soldo Y., Eybert-Berard L., and Menthonnex J.-J. (1998) Structural determination of Zn and Pb binding sites in *Penicillium chrysogenum* cell walls by EXAFS spectroscopy. *Environ. Sci. Technol.* **32**, 1648–1655.
- Segre C. U., Leyarovska N. E., Chapman L. D., Lavender W. M., Plag P. W., King A. S., Kropf A. J., Bunker B. A., Kemner K. M., Dutta P., Druan R. S., and Kaduk J. (2000) The MRCAT insertion device beamline at the Advanced Photon Source. In: *Synchrotron Radiation Instrumentation: Eleventh U.S. Conference* **CP521**, 419–422.

- Small T., Warren L. A., Roden E., and Ferris F. G. (1999) Sorption of strontium by bacteria, Fe(III) oxide, and bacteria-Fe(III) oxide composites. *Environ. Sci. Technol.* **33**, 4465–4470.
- Small T. D., Warren L. A., and Ferris F. G. (2001) Influence of ionic strength on strontium sorption to bacteria, Fe(III) oxide, and composite bacteria-Fe(III) oxide surfaces. *Appl. Geochem.* **11**, 547–554.
- Smith R. M., Martell A. E., and Motekaitis R. J. (1997) NIST critically selected stability constants of metal complexes database, version 4.0. In: *NIST Standard Reference Database*. Vol. 46. U.S. Department of Commerce.
- Stern E. A. (1993) Number of relevant independent points in X-ray-absorption fine-structure spectra. *Phys. Rev. B* **48**, 9825–9827.
- Stern E. A. and Heald S. M. (1983) Basic principles and applications of EXAFS. In *Handbook of Synchrotron Radiation*, Vol. 10 (ed. E. E. Koch), pp. 995–1014. North-Holland.
- Stern E. A., Newville M., Ravel B., Yacoby Y., and Haskel D. (1995) The UWXAFS analysis package: Philosophy and details. *Physica B* **208–209**, 2995–3009.
- Sturchio N. C., Antonio M. R., Soderholm L., Sutton S. R., and Brannon J. C. (1998) Tetravalent uranium in calcite. *Science* **281**, 971–973.
- Templeton D., Zalkin A., Ruben H., and Templeton L. (1985) Redetermination and absolute configuration of sodium uranyl(VI) triacetate. *Acta Cryst.* **C41**, 1439–1441.
- Thompson H. A., Brown G. E. Jr., and Parks G. A. (1995) Low and ambient temperature XAFS study of U(VI) in solids and aqueous solution. *Physica B* **208/209**, 167–168.
- Thompson H. A., Brown G. E. Jr., and Parks G. A. (1997) XAFS spectroscopic study of uranyl coordination in solids and aqueous solutions. *Am. Mineral.* **82**, 483–496.
- Westall J. C. (1982) FITEQL, A computer program for determination of chemical equilibrium constants from experimental data. Dept. Chem., Oregon St. Univ.
- Yee N. and Fein J. B. (2001) Cd adsorption onto bacterial surfaces: A universal adsorption edge? *Geochim. Cosmochim. Acta* **65**, 2037–2042.
- Zabinsky S. I., Rehr J. J., Ankudinov A., Albers R. C., and Eller M. J. (1995) Multiple-scattering calculations of X-ray-absorption spectra. *Phys. Rev. B* **52**, 2995–3009.